

Available online at [www.sciencedirect.com](http://www.sciencedirect.com)

ScienceDirect

journal homepage: [www.elsevier.com/locate/AJPS](http://www.elsevier.com/locate/AJPS)

## Research Article

# A biomimetic spore nanoplatform for boosting chemodynamic therapy and bacteria-mediated antitumor immunity for synergistic cancer treatment



Cuixia Zheng<sup>b</sup>, Lingling Sun<sup>e</sup>, Hongjuan Zhao<sup>a,c</sup>, Mengya Niu<sup>a</sup>, Dandan Zhang<sup>a</sup>, Xinxin Liu<sup>a</sup>, Qingling Song<sup>a</sup>, Weijie Zhong<sup>b</sup>, Baojin Wang<sup>d,\*</sup>, Yun Zhang<sup>a,c,\*</sup>, Lei Wang<sup>a,c,\*</sup>

<sup>a</sup> School of Pharmaceutical Sciences, Zhengzhou University, Zhengzhou 450001, China

<sup>b</sup> Huaihe Hospital of Henan University, Translational medicine Center, Kaifeng 475000, China

<sup>c</sup> Pingyuan Lab, Henan Normal University, Xinxiang 453007, China

<sup>d</sup> Gynecology, the Third Affiliated Hospital of Zhengzhou University, Zhengzhou 450052, China

<sup>e</sup> Weihai Municipal Hospital, Cheeloo College of Medicine, Shandong University, Weihai 264200, China

## ARTICLE INFO

## Article history:

Received 19 February 2024

Accepted 1 March 2024

Available online 24 April 2024

## Keywords:

Biomimetic spore shell

Bacteria-mediated antitumor therapy

Chemodynamic therapy

Immunotherapy

Tumor microenvironment

## ABSTRACT

Bacterial-based antitumor immunity has become a promising strategy to activate the immune system for fighting cancer. However, the potential application of bacterial therapy is hindered by the presence of instability and susceptibility to infections within bacterial populations. Furthermore, monotherapy is ineffective in completely eliminating complex cancer with multiple contributing factors. In this study, based on our discovery that spore shell (SS) of *Bacillus coagulans* exhibits excellent tumor-targeting ability and adjuvant activity, we develop a biomimetic spore nanoplatform to boost bacteria-mediated antitumor therapy, chemodynamic therapy and antitumor immunity for synergistic cancer treatment. In detail, SS is separated from probiotic spores and then attached to the surface of liposome (Lipo) that was loaded with hemoglobin (Hb), glucose oxidase (GOx) and JQ1 to construct SS@Lipo/Hb/GOx/JQ1. In tumor tissue, highly toxic hydroxyl radicals ( $\cdot\text{OH}$ ) are generated via sequential catalytic reactions: GOx catalyzing glucose into  $\text{H}_2\text{O}_2$  and  $\text{Fe}^{2+}$  in Hb decomposing  $\text{H}_2\text{O}_2$  into  $\cdot\text{OH}$ . The combination of  $\cdot\text{OH}$  and SS adjuvant can improve tumor immunogenicity and activate immune system. Meanwhile, JQ1-mediated down-regulation of PD-L1 and Hb-induced hypoxia alleviation synergistically reshape immunosuppressive tumor microenvironment and potentiate immune response. In this manner, SS@Lipo/Hb/GOx/JQ1 significantly suppresses tumor growth and metastasis. To summarize, the nanoplatform represents an optimum strategy to potentiate bacteria-based cancer immunotherapy.

© 2024 Shenyang Pharmaceutical University. Published by Elsevier B.V.

This is an open access article under the CC BY-NC-ND license

(<http://creativecommons.org/licenses/by-nc-nd/4.0/>)

\* Corresponding authors.

E-mail addresses: [wangbaojin@zzu.edu.cn](mailto:wangbaojin@zzu.edu.cn) (B. Wang), [zhangyun@zzu.edu.cn](mailto:zhangyun@zzu.edu.cn) (Y. Zhang), [wanglei1@zzu.edu.cn](mailto:wanglei1@zzu.edu.cn) (L. Wang).

Peer review under responsibility of Shenyang Pharmaceutical University.

<https://doi.org/10.1016/j.ajps.2024.100912>

1818-0876/© 2024 Shenyang Pharmaceutical University. Published by Elsevier B.V. This is an open access article under the CC BY-NC-ND license (<http://creativecommons.org/licenses/by-nc-nd/4.0/>)

## 1. Introduction

Cancer kills thousands of people every year and its treatment remains to face challenges all over the world [1]. Although conventional anticancer therapies (such as chemotherapy and radiation therapy) are still dominant, various emerging therapies open broad prospects in cancer therapy, such as chemodynamic therapy (CDT), immunotherapy and bacteria-mediated antitumor therapy (BMAT) [2-4]. Nonetheless, monotherapy always shows unsatisfactory therapeutic efficacy due to insufficient treatment response and generation of resistance [5,6]. Therefore, it is urgent to combine multiple therapies into a single regimen to explore innovation approaches for improved therapeutic efficacy. For instance, immunotherapy has been reported to enhance the antitumor efficacy when combined with other anticancer approaches such as chemotherapy, radiotherapy, BMAT and CDT [7-9].

One of the anticancer mechanisms of most antitumor treatments (chemotherapy, radiotherapy and CDT) is generating reactive oxygen species (ROS), which can increase tumor immunogenicity and activate antitumor immunity through various pathways [10-12]. On the one hand, ROS directly induce oxidative damage of cancer cells [13,14]. On the other hand, ROS could promote the activation of NOD-like receptor thermal protein domain associated protein 3 (NLRP3) inflammasomes, and further induce tumor cells to undergo pyroptosis, which has been proved to activate strong immune response [15,16]. However, unsatisfactory specificity of most therapeutic methods would induce unavoidable side effects and significantly impair therapeutic efficacy. Interestingly, CDT, which is defined as specific hydroxyl radicals ( $\cdot\text{OH}$ ) generation in cancer cells, induces lower side effects compared with other strategies [17]. Because transition metals, such as Fe, can decompose *in situ* hydrogen peroxide ( $\text{H}_2\text{O}_2$ ) into  $\cdot\text{OH}$ , which further activates antitumor immunity by inducing the release of danger-associated molecular pattern (DAMP), including adenosine triphosphate (ATP), high mobility group box 1 (HMGB1) and calreticulin (CRT) [18,19]. Although  $\cdot\text{OH}$  can induce immunogenic cell death (ICD) of tumor cells, the lack of immune adjuvants and immunosuppression compromises antitumor immunity [20].

Nowadays, BMAT has caught much attention owing to unique advantages of bacteria and their derivatives [21,22]. Recent research has revealed that locally infected bacteria can not only destroy tumor cells by producing bacterial toxins, but also boost antitumor immunity due to natural adjuvant components of bacteria [23-25]. Moreover, bacteria have excellent tumor-targeting ability due to their unique characteristics [26]. Yang's group reported that attenuated bacteria have been used as carriers to deliver therapeutic drugs for the enhancement of antitumor efficacy [23]. In addition to bacteria, many bacterial derivatives, such as spores and outer membrane vesicles, can also serve as vectors for drug delivery and adjuvants to activate the immune system [27-29]. However, there are still serious limitations for future application, such as the loss of cargo due to bacterial proliferation and bacteremia caused by bacterial infection [30,31]. Therefore, overcoming the above disadvantages while retaining tumor targeting ability

and adjuvant activity of bacteria remains a formidable challenge in BMAT. In previous work, we have successfully synthesized autonomous nanoparticles generator based on the hydrophobic component in spore shell (SS) of *Bacillus coagulans* [32]. This nanoplatform exhibited excellent tumor-targeting ability. However, it is uncertain whether the tumor-targeting effect is mediated by the components of SS.

Although antigens combined adjuvants can initiate robust immune response, interferon- $\gamma$  (IFN- $\gamma$ ) secreted by cytotoxic lymphocytes (CTLs) in tumors can promote upregulation of programmed cell death-ligand 1 (PD-L1) on tumor cells [33]. And PD-L1 can bind to programmed cell death protein 1 (PD-1) on the surface of CTLs and inactivate effector T cells, ultimately leading to adaptive resistance to immunotherapy [34,35]. JQ1, a bromodomain-containing protein 4 inhibitor (BRD4i), can selectively block PD-L1 and overcome immune resistance [2].

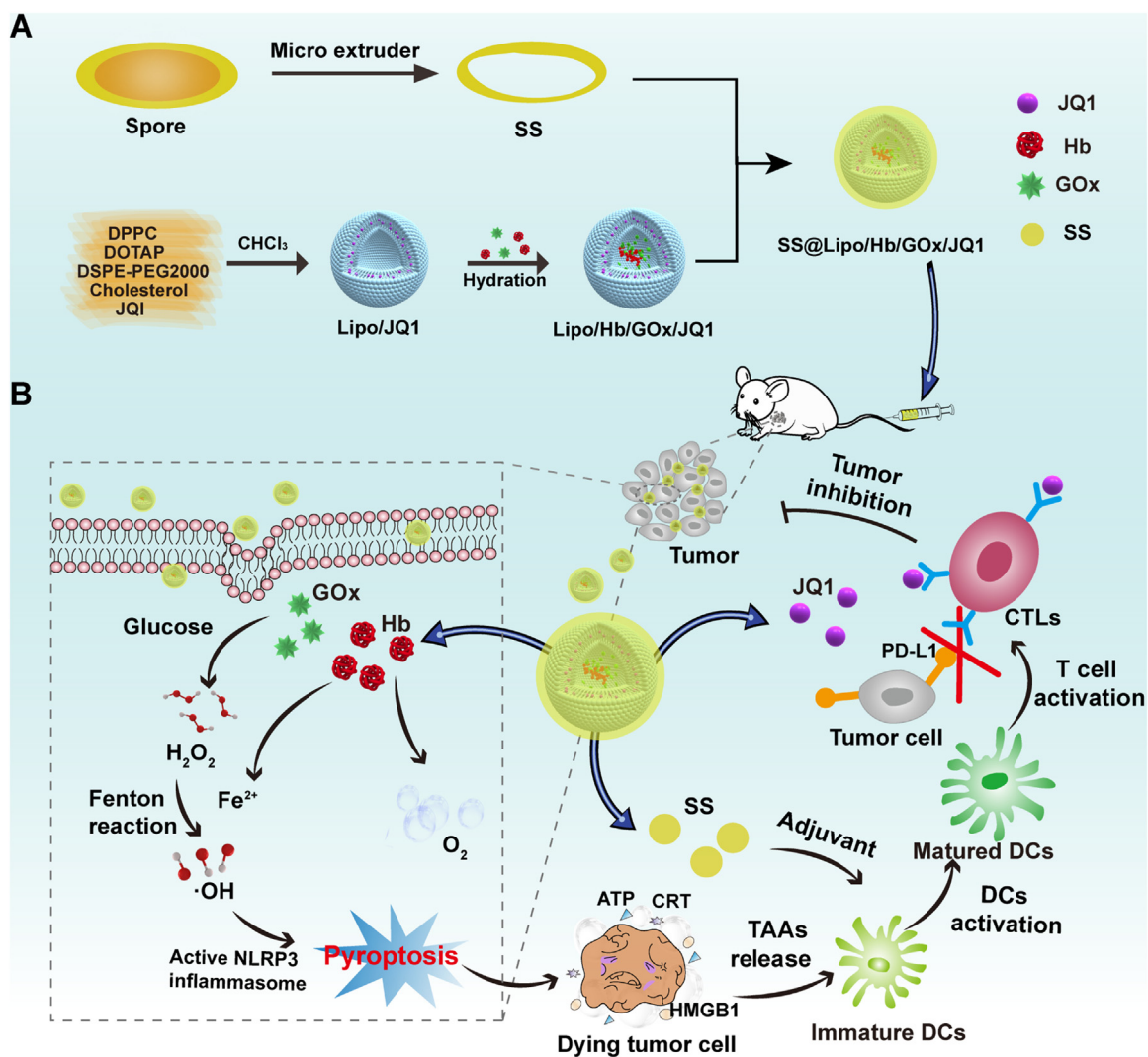
In this work, we separated the total SS using mechanical force and proved its tumor-targeting ability and adjuvant activity. Based on this discovery, we developed a SS biomimetic nanoplatform to boost BMAT, CDT and antitumor immunity for synergistic cancer treatment (Scheme 1). In detail, hemoglobin (Hb) and glucose oxidase (GOx) were encapsulated into the liposome (Lipo) containing JQ1 to construct Lipo/Hb/GOx/JQ1. Subsequently, SS@Lipo/Hb/GOx/JQ1 drug delivery system was obtained by attaching SS to the surface of Lipo/Hb/GOx/JQ1. After reaching tumor tissue, GOx could catalyze glucose in tumor region into abundant  $\text{H}_2\text{O}_2$ , which was decomposed into liberate highly toxic  $\cdot\text{OH}$  by  $\text{Fe}^{2+}$  in Hb. The generated  $\cdot\text{OH}$  triggered oxidative damage of tumor cells and promoted the activation of NLRP3 inflammasome, thereby inducing tumor cells to undergo pyroptosis and releasing tumor-associated antigens (TAAs). Notably, the combination of TAAs and SS adjuvant boosted dendritic cells (DCs) maturation and enhanced intratumoral  $\text{CD8}^+$  T lymphocytes antitumor activity. Furthermore, targeted inhibition of BRD4 with JQ1 significantly down-regulated the transcription of PD-L1, thus suppressing immune evasion. In addition, Hb, as a good oxygen donor, could increase the oxygen concentration in tumor microenvironment (TME) and weaken hypoxia-encouraged immune suppression. Collectively, the nanoplatform might be an optimum strategy to potentiate cancer immunotherapy.

## 2. Materials and methods

### 2.1. Materials

1,2-dihexadecanoyl-rac-glycero-3-phosphocholine (DPPC), cholesterol, 1,2-dioleoyl-3-trimethylammonium-propane (DOTAP) and 2-distearyl-sn-glycero-3-phosphoethanolamine (DSPE-PEG2000) were obtained from Corden Pharma. Hb was purchased from Macklin (Shanghai, China). GOx and dihydrochloride (DAPI) were acquired from Sigma-Aldrich. JQ1 was obtained from MCE (China) and C11-BODIPY581/591 from Thermo Fisher Scientific (USA).

4T1 breast tumor cells were obtained from Shanghai Cell Bank, Chinese Academy of Sciences (CAS). Complete RPMI



**Scheme 1 – Schematic illustration of anti-tumor mechanism of SS@Lipo/Hb/GOx/JQ1.**

1640 supplemented with 10 % fetal bovine serum (BI, South America) at 37 °C and 5 % CO<sub>2</sub> was employed to culture cells.

BALB/c mice (female, 4–6 weeks) and SD rats (180 ± 20 g) were bought from Zhengzhou Laboratory Animal Center. Animal experiments complied with experiments were performed based on principles of Experimental Animals Administrative Committee of Zhengzhou University.

## 2.2. Preparation and characterization of SS@Lipo/Hb/GOx/JQ1

Firstly, *Bacillus coagulans* were cultured and their spores were separated according to our previous literature [32]. For the preparation of the SS, the spore solution was diluted to 0.5 mg/ml and then extruded back and forth 13 times through polycarbonate membrane with pore size of 800 nm using a micro extruder. Next, SS was obtained after centrifugation (5,000 rpm, 10 min). The morphologies of spore and SS were characterized by transmission electron microscope (TEM, HT7700, Japan).

For the preparation of SS@Lipo/Hb/GOx/JQ1, DPPC, DOTAP, cholesterol, DSPE-PEG2000 and JQ1 (14:2:1:0.2:2.15, mass

ratio) were dissolved in chloroform. After chloroform was evaporated, a mixed solution of Hb and GOx was used to hydrate the lipid film. After sonication (200 W, 3/5 s on/off) for 180 s, the final Lipo/Hb/GOx/JQ1 was prepared. After treatment with probe sonication (300 W, 3/5 s on/off) for 30 min, SS was mixed with Lipo/Hb/GOx/JQ1. The mixed solution was extruded 11 times with a sequential pore size of 400 nm and 200 nm to obtain SS@Lipo/Hb/GOx/JQ1.

Dynamic light scattering (DLS) analyzer (Zetaster, Malvern, UK) and TEM were used to detect the size distribution/zeta potential and morphology of SS@Lipo/Hb/GOx/JQ1. The concentration of JQ1 was measured by high-performance liquid chromatography (HPLC). The separation and detection conditions were as follows: Venusil XBP C<sub>18</sub> column (4.6 mm × 150 mm, 5 μm) at 30 °C for separation, water and acetonitrile (25:75, 1 ml/min) as isocratic mobile phase. The measuring wavelength was set at 254 nm, and the injection volume was 20 μl. The concentration of Hb was determined at 405 nm by an ultraviolet-visible (UV/Vis) spectrophotometer (Shimadzu, Tokyo, Japan). For the detection of GOx, GOx-FITC was first synthesized through protein bonding. Then, the concentration of fluorescein isothiocyanate (FITC) was

measured via fluorescence spectrophotometry (Ex: 488 nm, Em: 514 nm) and Gox concentration was calculated according to bonding efficiency.

### 2.3. *In vitro cellular uptake*

After incubation in 6-well plates for 24 h, 4T1 cells were treated with FITC, Lipo/FITC, SS@Lipo/FITC. After 1, 2 or 4 h incubation, DAPI was used to label nucleus, and the fluorescence was detected with confocal laser scanning microscope (CLSM) (Leica, Germany) and flow cytometry.

### 2.4. *Intracellular ROS measurement and lipid peroxidation detection*

After 4T1 cells treatment with PBS, SS@Lipo, Hb+GOx, SS@Lipo/Hb/GOx and SS@Lipo/Hb/GOx/JQ1 (Hb: 50 µg/ml, GOx: 0.1 µg/ml and JQ1: 50 µg/ml) for 24 h, 2,7-dichlorodihydrofluorescein diacetate (DCFH-DA) was used for the detection.

The intracellular lipid peroxide initiated by SS@Lipo/Hb/GOx/JQ1 was determined by CLSM. 4T1 cells in a confocal dish were treated with PBS, SS@Lipo, Hb+GOx, SS@Lipo/Hb/GOx and SS@Lipo/Hb/GOx/JQ1 (Hb: 50 µg/ml, GOx: 0.1 µg/ml and JQ1: 50 µg/ml), respectively. After 24 h, the cells were incubated with C11-BODIPY<sup>581/591</sup> (2 µM) for 30 min and subsequently observed via CLSM.

### 2.5. *In vitro antitumor performance of SS@Lipo/Hb/GOx/JQ1*

4T1 cells were treated with PBS, SS@Lipo, Hb+Gox, SS@Lipo/Hb/GOx and SS@Lipo/Hb/GOx/JQ1. After incubation for 24 h, cell viability was measured by MTT method.

After the cell incubation with PBS, SS@Lipo, Hb+Gox, SS@Lipo/Hb/GOx and SS@Lipo/Hb/GOx/JQ1 (Hb: 50 µg/ml, GOx: 0.1 µg/ml and JQ1: 50 µg/ml) for 24 h, the cells were treated with Calcein AM/PI according to directions and observed by using fluorescence microscope.

### 2.6. *In vitro pyroptosis assay*

4T1 cells were incubated with PBS, SS@Lipo, Hb+Gox, SS@Lipo/Hb/GOx and SS@Lipo/Hb/GOx/JQ1 (Hb 50 µg/ml, GOx 0.1 µg/ml, JQ1 50 µg/ml) for 24 h. The cell morphology was observed and photographed by electron microscope. Meanwhile, the cell supernatant was collected to detect interferon-1β (IL-1β) and lactic dehydrogenase (LDH) with enzyme-linked immunosorbent assay (ELISA) and LDH Release Assay Kit (Beyotime Biotechnology), respectively. The expression of the pyroptosis marker NLRP3 was evaluated by western blotting.

### 2.7. *In vitro tumor immunogenicity detection*

4T1 cells were incubated with PBS, SS@Lipo, Hb+Gox, SS@Lipo/Hb/GOx and SS@Lipo/Hb/GOx/JQ1 (Hb 50 µg/ml, GOx 0.1 µg/ml, JQ1 50 µg/ml) for 24 h. For CRT measurement, the cells were fixed with pre-chilled 75 % ethanol, incubated with anti-CRT antibody, stained with DAPI and observed

with CLSM. Meanwhile, the cell supernatant was collected for HMGB1 measurement via ELISA kit according to directions.

Moreover, bone marrow-derived dendritic cells (BMDCs) were prepared according to previous literature [2]. After 4T1 cells incubation with different formulations (Hb 50 µg/ml, Gox 0.1 µg/ml, JQ1 50 µg/ml) for 24 h, cell supernatant was collected and added to BMDCs for their maturation. After 24 h, BMDC cells were collected and incubated with anti-CD86-FITC and anti-CD40-APC antibodies, and analyzed by flow cytometry (BD, USA).

### 2.8. *In vivo biodistribution*

Tumor-bearing mice (female, 4–6 weeks, BALB/c) were randomly divided into 3 groups and injected (i.v.) with free IR780, Lipo/IR780 and SS@Lipo/IR780 at equal amounts of IR780 after two weeks. Subsequently, IR780 distribution was observed by a living imaging system (Bruker, Germany) at a set time points. After 24 h, major organs and tumor tissue were extracted to detect the fluorescence intensity of IR780.

### 2.9. *Pharmacokinetic study*

To investigate the pharmacokinetics of SS@Lipo/Hb/GOx/JQ1, Sprague Dawley (SD) rats (female, 180 ± 20 g) were i.v. injected with JQ1, Lipo/Hb/GOx/JQ1 and SS@Lipo/Hb/GOx/JQ1 solution at an identical JQ1 dose of 15.0 mg/kg. Blood samples were collected and processed at the estimated time point post-injection. The blood concentration of JQ1 was quantitatively examined using HPLC.

### 2.10. *In vivo anticancer efficacy*

BALB/c mice were subcutaneously injected  $1 \times 10^6$  4T1 cells. When volume of tumor was about 100 mm<sup>3</sup>, the mice were randomly divided into 5 groups (n = 5): control, SS@Lipo, Hb+GOx, SS@Lipo/Hb/GOx and SS@Lipo/Hb/GOx/JQ1 (Hb: 15 mg/kg, GOx: 2 mg/kg, and JQ1: 15 mg/kg). Tumor volume and body weight of mice were recorded every other day. The tumor tissues and major organs were used for hematoxylin-eosin (H&E) staining post whole treatments. Furthermore, Ki67, terminal deoxynucleotidyl transferase dUTP nick end labeling (TUNEL), hypoxia-inducible factor-1α (HIF-1α), gasdermin-D (GSDMD), HMGB1, CRT, PD-L1 and CD8 in tumor tissues were detected via immunofluorescence and immunohistochemical staining.

### 2.11. *Tumor immune infiltration and cytokine secretion*

After tumor-bearing mice treatment with saline, SS@Lipo, Hb+GOx, SS@Lipo/Hb/GOx and SS@Lipo/Hb/GOx/JQ1 3 times, tumor tissues and lymph nodes were collected and digested into single-cell suspensions. The obtained cells were stained with Dead/Live-FVS620, Fc block, anti-CD45-APC-Cy7, anti-CD3-BV510, anti-CD11b-BB515, anti-CD11c-BV605, anti-F4/80-BV421, anti-CD86-APC-R700, anti-CD40-PE, anti-CD4-PE, anti-CD8-PerCP-Cy5, and anti-Foxp3-BV421 antibodies at 4 °C for 30 min. Next, the cells were measured by flow cytometry. Meanwhile, the serum levels of interleukin-6 (IL-6), IFN-γ and

tumor necrosis factor  $\alpha$  (TNF- $\alpha$ ) were detected with ELISA kits on Synergy Neo microplate reader (BioTek, USA).

### 2.12. Lung metastatic analysis

4T1-bearing mice were treated with different formulations as described in "2.1.10 *In vivo* anticancer efficacy". After 40 d, the lung tissues were collected from sacrificial mice and subjected to H&E staining for lung metastatic analysis.

### 2.13. *In vivo* biosafety study

Firstly, healthy mice were injected (*i.v.*) with saline, lipopolysaccharide (LPS, *i.v.*, 500  $\mu$ g/ml, 100  $\mu$ l) and SS (*i.v.*, 5 mg/kg). Subsequently, the body temperatures of mice were detected with electric thermometer (FR1DZ1, Microlife, Switzerland). Next, SD rats (180  $\pm$  20 g,  $n$  = 3) were administrated with saline and SS (*i.v.*, 5 mg/kg), respectively. After 48 h, blood samples of rats were collected for routine blood, coagulation indexes, C-reactive protein (CRP), procalcitonin (PCT), and blood biochemical indices examinations.

Healthy mice were injected (*i.v.*) with PBS, SS@Lipo, SS@Lipo/Hb/GOx and SS@Lipo/JQ1/Hb/GOx (Hb: 15 mg/kg, GOx: 2 mg/kg, and JQ1: 15 mg/kg). After treatment with different formulations 5 times, blood biochemical parameters were measured to evaluate biosafety of the nanoplatform.

### 2.14. Statistical analysis

Data represent mean  $\pm$  standard deviation (SD) from at least three independent replicates. Statistical difference was assessed by one-way ANOVA, two-way ANOVA, and t-test. Significance was indicated by  $P$  values  $<$  0.05,  $<$  0.01, and  $<$  0.001.  $P$   $<$  0.05 was regarded as significant.

## 3. Results and discussion

### 3.1. Preparation and characterization of SS

For the preparation of SS, spores were first separated from *Bacillus coagulans*. Next, the contents of spores were removed through mechanical force by a liposome extrusion instrument to obtain SS, according to our previous report [36]. The size distribution and zeta potential of SS showed no significant difference with spores (Fig. S1). According to TEM in Fig. 1A, SS showed similar appearance and size in comparison with spores, but the main contents of SS vanished from sight, indicating that SS with the purity of around 95.3 % was successfully isolated from spores. Next, the distribution and proportion of different elements (C, N, O, Ca, Mn, P, S, Zn) were analyzed by elemental mapping. The results in Figs. 1B and S2 indicated that C, N, O, Ca, Mn and P were dominant metal populations in SS. Moreover, the amount of peptidoglycan (PGN) in SS was examined by ELISA and calculated to be 60  $\mu$ g/mg.

To investigate the immunological effect of SS, CRT and HMGB1 in 4T1 mouse breast cancer cells were detected post-treatment with SS. As demonstrated in Fig. 1C and D,

both the CRT and HMGB1 levels did not significantly change after treatment with SS, suggesting that SS had no influence on immunogenicity of tumor cells. However, SS treatment significantly upregulated the expression of CD86 and CD40 on BMDCs (Fig. 1E), demonstrating its capacity in promoting BMDCs maturation. These results might attribute to adjuvant components inherited from the parent spores, such as PGN and Mn, which could enhance the immune response through toll-like receptor 2 (TLR2) and cyclic guanosine monophosphate-adenosine monophosphate synthetase stimulator of interferon genes (cGAS-STING) pathways, respectively [37,38].

Before application, we investigated the biosecurity of SS via a series of experiments. At first, hemolysis test was detected, and the results in Fig. S3 indicated negligible hemoglobin release and low hemolysis rate ( $<$  5 %). After intravenous administration of SS, body temperature of mice did not rise compared to the mice treated with LPS, maintaining consistency with healthy mice (Fig. S4). Then, routine blood assays revealed that white blood cells (WBC), red blood cells (RBC), blood platelet (PLT), hemoglobin (HGB) and hematocrit (HCT) showed no significant difference with healthy mice (Fig. 1F). To further investigate systemic toxicity, serum samples were collected for detection of CRP and PCT. The results in Fig. 1G demonstrated that SS induced no systemic infection or plasmic immune reaction. The above results indicated that SS would not induce acute and short-term microbiological infection. Moreover, coagulation indexes, such as D-D level, fibrinogen (FBG) and thrombin time (TT), were measured, which identified no risk of thrombosis after administration of SS (Fig. 1H). Finally, the results of liver function (alanine transaminase, ALT; aspartate aminotransferase, AST) and kidney function (creatinine, CREA; UREA) indicated negligible damage on renal and hepatic functions (Fig. S5). Therefore, inappreciable systemic toxicity was exhibited after treatment with SS, suggesting its good biosecurity for further application.

After detecting the biosafety of SS, we investigated whether SS inherited tumor targeting properties from the parental spores with Lipo as control. We first confirmed the attachment of SS onto the surface of Lipo via TEM (Fig. 1J). Then, the biodistribution of free IR780, Lipo/IR780 and SS@Lipo/IR780 was evaluated in 4T1-bearing BALB/c mice by using the fluorescence imaging system. Compared with free IR780, Lipo/IR780 and SS@Lipo/IR780 showed distinct fluorescence signal at tumor site 8 h post-injection (Fig. 1K). After 24 h, the fluorescence intensity of SS@Lipo/IR780 at isolated tumor site was obviously stronger than that of Lipo/IR780, as shown in Fig. S6. These results demonstrated that the SS inherited tumor-targeting property from the parent spores, such as peptidoglycan, which could recognize the TLR2 receptor, which is highly expressed in tumor sites [39]. We envisioned that SS could be used to develop functional nanoplatforms for bacteria-mediated antitumor immunity.

### 3.2. Preparation and characterization of SS@Lipo/Hb/GOx/JQ1

Considering that SS had no influence on tumor immunogenicity but could act as an immune adjuvant,

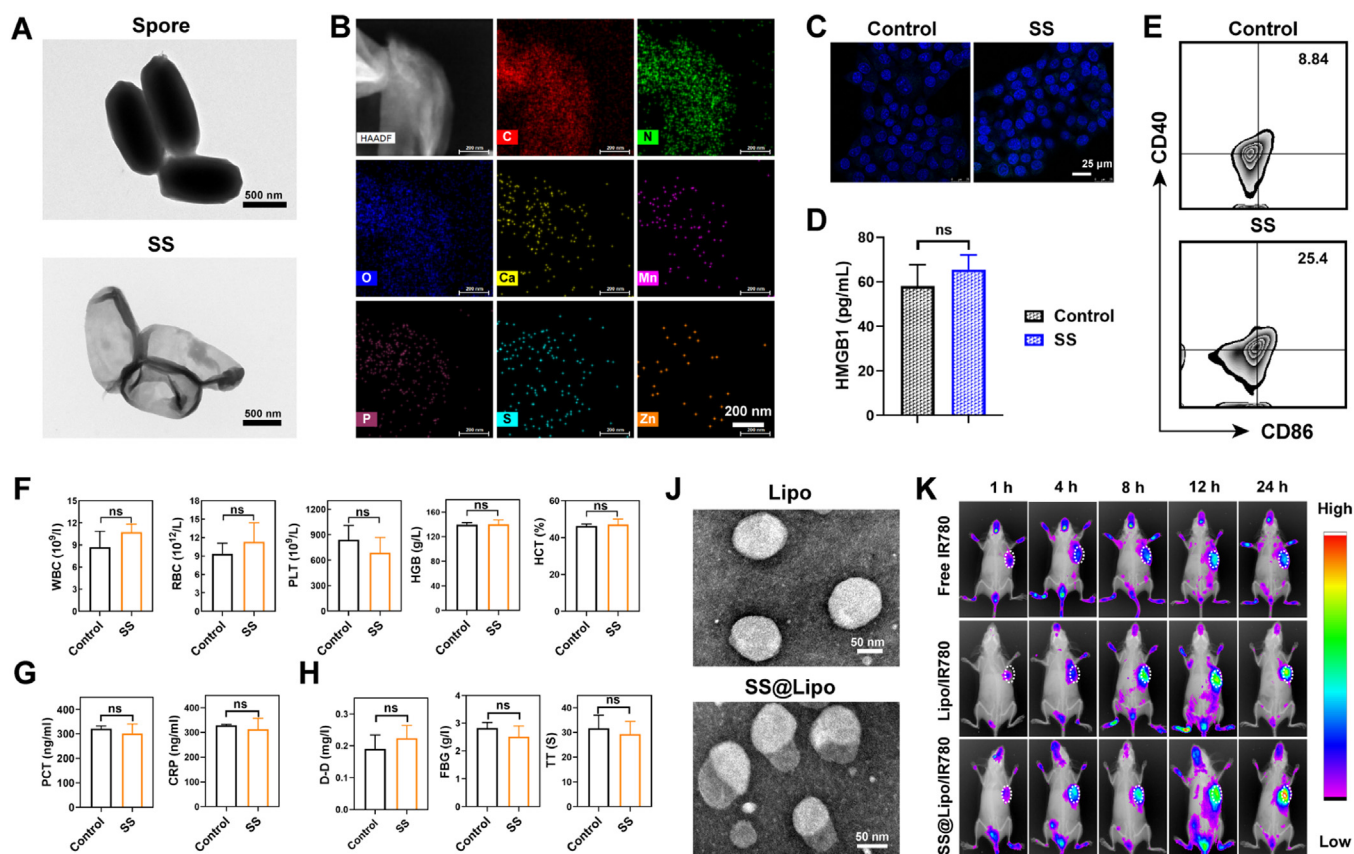


**Fig. 1 – (A)** TEM images of *Bacillus coagulans* spore and SS. **(B)** HAADF images of SS. **(C)** CRT expression in 4T1 breast cancer cells. **(D)** HMGB1 release from 4T1 cells after incubation with SS. **(E)** BMDCs maturation (CD40+CD86+) after incubated with SS. **(F)** Blood biochemistry of in healthy mice after administration with saline and SS. **(G)** PCT and CRP detection. **(H)** D-D level, FBG and TT in serum of rat. **(I)** TEM images of Lipo and SS@Lipo. **(K)** Near-infrared fluorescence imaging. Data are presented as mean  $\pm$  SD ( $n = 3$ ); ns = nonsignificant; P values were calculated by t-test.

as proved in the above experiments, we intended to improve the tumor immunogenicity by inducing ICD via ROS/NLRP3 inflammasomes activation-mediated pyroptosis for enhanced antitumor immunity. To avoid damage to normal tissues, in situ chemical reactions were used to provide highly toxic  $\cdot\text{OH}$ . As shown in Fig. S7, iron ions in Hb could convert  $\text{H}_2\text{O}_2$  into  $\cdot\text{OH}$ , which could transform methylene blue (MB) from a blue to a colorless form, accompanied by the disappearance of characteristic absorption in UV/vis spectrum. When GOx catalyzed glucose oxidation to boost  $\text{H}_2\text{O}_2$  generation, the amount of  $\cdot\text{OH}$  increased with the increase of Hb concentration (Fig. S8). Therefore, intracellular glucose could serve as a substrate to generate  $\text{H}_2\text{O}_2$  for considerable  $\cdot\text{OH}$  to achieve satisfying therapeutic efficacy.

To develop antitumor nanoplatform, Hb, GOx and JQ1 were encapsulated with Lipo to construct Lipo/Hb/GOx/JQ1. Then, SS was attached to the surface of Lipo/Hb/GOx/JQ1 via electrostatic interactions to obtain SS@Lipo/Hb/GOx/JQ1. As the TEM images in Fig. 2A displayed, both Lipo/Hb/GOx/JQ1 and SS@Lipo/Hb/GOx/JQ1 were of good morphology. The average hydrodynamic diameter and zeta potential of different nanoplatforms were measured by DLS. The particle size of SS@Lipo/Hb/GOx/JQ1 ( $\sim 121.6$  nm) was

**Table 1 – The encapsulation efficiency and drug loading efficiency of Hb, GOx and JQ1.**

	Hb	GOx	JQ1
Encapsulation efficiency	76.3 % $\pm$ 1.9 %	43.7 % $\pm$ 2.4 %	67.5 % $\pm$ 2.6 %
Drug loading efficiency	16.12 % $\pm$ 2.1 %	1.23 % $\pm$ 0.5 %	14.28 % $\pm$ 1.3 %

slightly increased than that of Lipo/JQ1/Hb/GOx ( $\sim 102.7$  nm) (Fig. S9A). As shown in Fig. S9B, the zeta potentials of Lipo/JQ1/Hb/GOx and SS@Lipo/Hb/GOx/JQ1 were around +5.4 mV and  $-19.2$  mV, respectively, and the later was in line with that of SS ( $-24.7$  mV). Increased particle size and surface charge variations proved attachment of SS to Lipo/Hb/GOx/JQ1. Moreover, the UV/Vis absorption peaks at 254 nm, 405 nm and 495 nm were consistent with the maximum absorption peaks of free JQ1, Hb and GOx-FITC, confirming the successful preparation of SS@Lipo/Hb/GOx/JQ1 (Fig. S10). The encapsulation efficiency and drug loading efficiency of Hb, GOx and JQ1 were calculated and the results were displayed in Table 1.

Next, the release profile of GOx and Fe ions was detected in different mediums. As shown in Fig. S11A, the cumulative

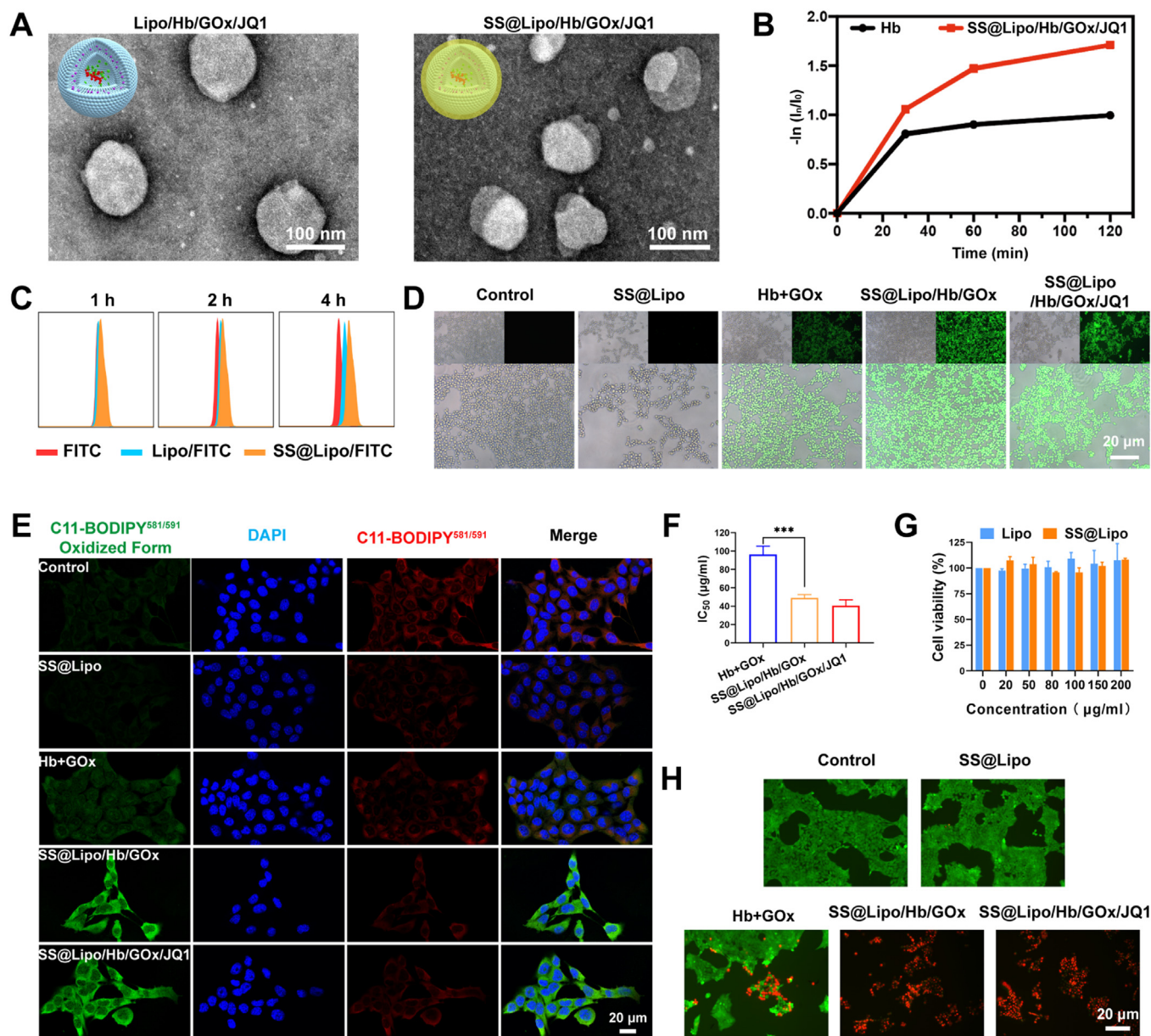


**Fig. 2 – (A)** TEM images of Lipo/JQ1/Hb/GOx and SS@Lipo/Hb/GOx/JQ1. **(B)** The oxygen release capability of free Hb and SS@Lipo/Hb/GOx/JQ1.  $I_0$  and  $I_n$  represented the fluorescence  $\text{Ru}(\text{dpp})_3\text{Cl}_2$  intensity of (fluorescence quenching  $\text{O}_2$  probe) before and after reaction, respectively. **(C)** Cellular internalization of free FITC, Lipo/FITC and SS@Lipo/FITC in 4 T1 cells. **(D)** Detection of ROS with DCFH-DA. **(E)** CLSM images of lipid peroxidation in different groups. **(F)**  $\text{IC}_{50}$  of different formulations ( $n = 3$ ; mean  $\pm$  SD). **(G)** Cell viability curves after incubation with Lipo and SS@Lipo ( $n = 3$ ; mean  $\pm$  SD). **(H)** Staining of live/dead cells. P values were calculated by one-way ANOVA with a Tukey post-hoc test (\*\*\* $P < 0.001$ ).

release percentage of GOx from Lipo/Hb/GOx/JQ1 and SS@Lipo/Hb/GOx/JQ1 in simulated TME were around 78.89 % and 69.49 % respectively, demonstrating no significant difference. For Fe, the release percentage was only about 27.8 % after 24 h incubation at pH 6.0. After adding  $\text{H}_2\text{O}_2$  (1 mM) into medium, the cumulative release percentage rapidly reached to 55.08 % (Fig. S11B), which was mainly attributed to the possibility that Fe ions in Hb could be released into solution in the presence of  $\text{H}_2\text{O}_2$ . In the presence of glucose, SS@Lipo/Hb/GOx/JQ1 continuously

decreased UV/Vis absorption of MB at 665 nm (Fig. S12), indicating the continuous generation of  $\cdot\text{OH}$ . Negligible changes in particle size, PDI and zeta potential demonstrated superior stability of SS@Lipo/JQ1/Hb/Gox (Fig. S13). Next, we investigated oxygen release capability of SS@Lipo/Hb/Gox/JQ1 with  $(\text{Ru}(\text{dpp})_3\text{Cl}_2)$  as  $\text{O}_2$  indicator [40]. As shown in Fig. 2B, the oxygen amount released by SS@Lipo/Hb/Gox/JQ1 was noticeably higher than that of free Hb, which was mainly due to the improved stability of Hb in the nanoplatform.

### 3.3. *In vivo* antitumor performance of SS@Lipo/Hb/Gox/JQ1

Given the tumor targeting property of SS, we evaluated the cellular uptake efficiency of FITC labeled nanoplatform to confirm whether SS could increase the intracellular delivery of antitumor agents. Flow cytometry in Fig. 2C and CLSM examination in Fig. S14 illustrated that both Lipo/FITC and SS@Lipo/FITC induced growing fluorescence signal within 4T1 cells over time. By comparison, intracellular fluorescence intensity in SS@Lipo/FITC group was higher than that of Lipo/FITC group at all time points, which might be due to the function of one or more proteins in SS.

To verify whether SS@Lipo/Hb/Gox/JQ1 elevated intracellular ROS level, DCFH-DA was used to detect ROS. As shown in Fig. 2D and S15, no green fluorescence was observed in control and SS@Lipo groups. Tumor cells exhibited moderate intensity of the green fluorescence after treatment with Hb+Gox. While SS@Lipo/Hb/Gox and SS@Lipo/Hb/Gox/JQ1 significantly increased intracellular fluorescence intensity. In addition, lipid peroxide level was monitored via the lipid peroxidation probe C11-BODIPY<sup>581/591</sup>, the fluorescence of which shifted from red (C11-BODIPY<sup>581/591</sup>) to green (C11-BODIPY<sup>488/510</sup>) [41]. As shown in Fig. 2E, SS@Lipo/Hb/Gox and SS@Lipo/Hb/Gox/JQ1 led to the loss of C11-BODIPY<sup>581/591</sup> red fluorescence and the increase of C11-BODIPY<sup>488/510</sup> green fluorescence in 4T1 cells, consistent with intracellular ROS level.

Next, cytotoxic effect of Hb+Gox was examined by MTT assay. As indicated in Fig. 2F, IC<sub>50</sub> of Hb decreased from 85 to 41 µg/ml. However, SS@Lipo showed almost no cytotoxicity to tumor cells after 24 h co-incubation, even at a concentration of up to 200 µg/ml (Fig. 2G). These results demonstrated that increasing delivery of intracellular antitumor agents by SS-based nanoplatform could achieve high therapeutic efficacy at low drug doses, which was meaningful in reducing side effects in cancer treatment. Moreover, live/dead staining experiments (Fig. 2H) also demonstrated that SS@Lipo/Hb/Gox/JQ1 exhibited high efficiency in killing tumor cells by oxidative damage and starvation therapy [42].

To gain deep insights into the antitumor mechanism, SS@Lipo/Hb/Gox/JQ1-induced pyroptosis was investigated. As indicated in Fig. 3A, large bubbles from cancer cell membranes were clearly observed with an optical microscope after treatment with Hb+GOx, SS@Lipo/Hb/Gox and SS@Lipo/Hb/Gox/JQ1. The number of cells undergoing pyroptosis process was much higher in SS@Lipo/Hb/Gox and SS@Lipo/Hb/Gox/JQ1 groups than that in Hb+GOx group. Subsequently, IL-1 $\beta$  and LDH released by tumor cells were monitored to further testify the pyroptosis process. As shown in Fig. 3B, compared with other groups, IL-1 $\beta$  and LDH levels in the supernatant were significantly increased after treatment with SS@Lipo/Hb/Gox and SS@Lipo/Hb/Gox/JQ1. Moreover, the pyroptosis marker NLRP3 was evaluated after different treatments. As shown in Fig. S16, the western blot and semiquantitative results certified that NLRP3 expression obviously increased after treatment with SS@Lipo/Hb/Gox and SS@Lipo/Hb/Gox/JQ1, further demonstrating that

biomimetic spore nanoplatform could induce pyroptosis of tumor cells.

### 3.4. *In vitro* SS@Lipo/Hb/Gox/JQ1 enhanced tumor immunogenicity

It has been reported that pyroptosis can activate immune system by promoting the recognition of tumor antigens to antigen-presenting cells (APCs) [43]. Next, we assessed CRT exposure and HMGB1 release of cancer cells after different treatments. As displayed in Fig. 3C, CRT expression on dying tumor cells was obviously upregulated after treatment with SS@Lipo/Hb/Gox and SS@Lipo/Hb/Gox/JQ1. Meanwhile, HMGB1 release (Fig. 3D) also confirmed the capability of SS@Lipo/Hb/Gox/JQ1 to initiate immune response. It has been reported that increased tumor immunogenicity could activate APCs to trigger an immune response for fighting against tumor (Fig. 3E). After incubating BMDCs with the supernatant of tumor cells that were treated with various formulations, ICD-induced DCs maturation was investigated by detecting the CD86 and CD40 expression. From flow cytometry analysis (Fig. 3F), the ratio of mature DCs (CD86+CD40+) in SS@Lipo, Hb+GOx, SS@Lipo/Hb/Gox and SS@Lipo/Hb/Gox/JQ1 group was around 2.6-, 2.3-, 4.2- and 4.4-fold higher than that of control group.

### 3.5. *In vivo* antitumor performance of SS@Lipo/Hb/Gox/JQ1

At first, we investigated the circulation time of SS@Lipo/Hb/Gox/JQ1 via pharmacokinetic experiments. SD rats were i.v. administrated JQ1, Lipo/Hb/Gox/JQ1 and SS@Lipo/Hb/Gox/JQ1. Subsequently, blood samples were collected at pre-estimated points for detection of JQ1 concentrations. In comparison with free JQ1, both Lipo/Hb/Gox/JQ1 and SS@Lipo/Hb/Gox/JQ1 significantly prolonged the blood clearance half-life ( $T_{1/2}$ ) and promoted the area under curves ( $AUC_{0-t}$ ) of JQ1 (Fig. S17). However, the  $T_{1/2}$  and  $AUC_{0-t}$  between Lipo/Hb/Gox/JQ1 and SS@Lipo/Hb/Gox/JQ1 had no obvious difference. The pharmacokinetic profiles demonstrated that the nanoplatform could significantly elongate blood circulation of free drug.

Next, we further investigated the *in vivo* antitumor efficacy of SS@Lipo/Hb/Gox/JQ1. Tumor-bearing mice (~100 mm<sup>3</sup>) were randomly divided into five groups ( $n = 5$ ): i.v. administrated saline, SS@Lipo, Hb+GOx, SS@Lipo/Hb/Gox and SS@Lipo/Hb/Gox/JQ1 at a dose of Hb (15 mg/kg), GOx (2 mg/kg) and JQ1 (15 mg/kg). As depicted in Figs. 4A and S18, SS@Lipo could hardly inhibit tumor growth, and Hb+GOx exhibited modest antitumor effect, consistent with *in vitro* results. By comparison, SS@Lipo/Hb/Gox and SS@Lipo/Hb/Gox/JQ1 displayed outstanding tumor inhibition efficacy. Moreover, the relative tumor volume of SS@Lipo/Hb/Gox/JQ1 was significantly lower than that of SS@Lipo/Hb/Gox. Post-treatment analysis of tumor inhibition was investigated by H&E staining and TUNEL fluorescence staining. Closely arranged tumor cells with complete morphology were clearly observed after treatment with saline and SS@Lipo, as depicted in Fig. 4B. On the contrary, maximum apoptotic cells with

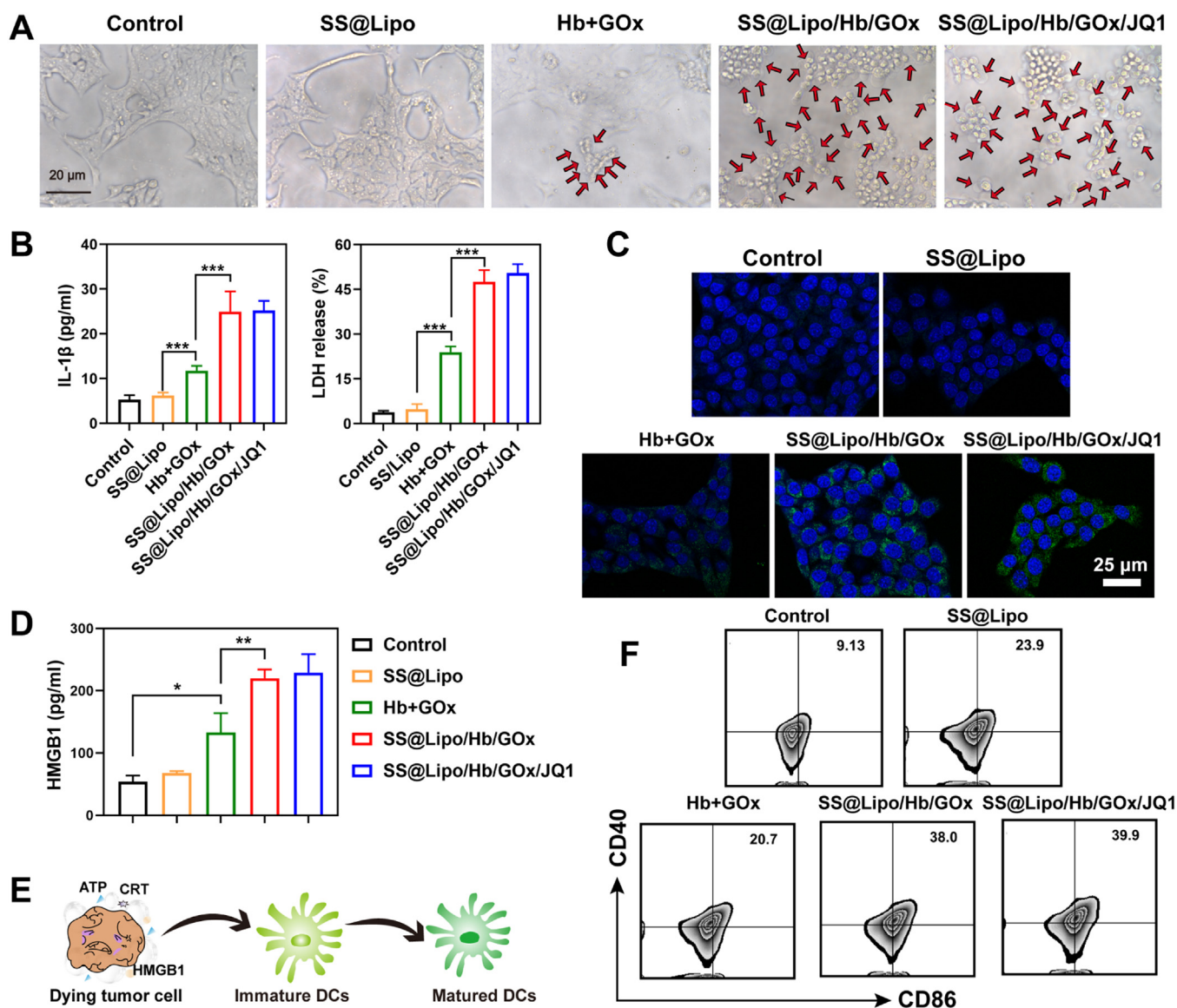


**Fig. 3 – (A) Images of 4T1 cells; Arrows, the pyroptotic cells. (B) The release of IL-1 $\beta$  and LDH. (C). CLSM images of CRT in 4T1 cells. (D) Release of HMGB1. (E) Schematic illustration of mechanism of DCs maturation. (F) Examination of DC maturation (CD86+CD40+) by flow cytometry after treatment with various formulations. Data are presented as mean  $\pm$  SD ( $n = 3$ ); \* $P < 0.05$ , \*\* $P < 0.01$  and \*\*\* $P < 0.001$ , calculated by one-way ANOVA with a Tukey post-hoc test.**

concentrated nucleus were observed in SS@Lipo/Hb/GOx and SS@Lipo/Hb/GOx/JQ1 groups. During the entire treatment period, no obvious weight loss was found in all groups (Fig. S19). Moreover, no inflammation and damage were observed in major tissues from the H&E staining (Fig. S20), suggesting good biocompatibility of the nanoplatform. Meanwhile, there was no obvious abnormality in blood and biochemical detection after various administrations (Fig. S21), further confirming negligible toxicity of the nanoplatform.

Hypoxia is a critical microenvironmental factor responsible for impaired antitumor immune response [44]. Reshaping the hypoxic immune suppressive TME has been reported to be an effective way to improve cancer immunotherapy [45,46]. Immunohistochemical study (Fig. 4C) displayed that the expression of HIF-1 $\alpha$

was significantly down-regulated after treatment with Hb+GOx, SS@Lipo/Hb/GOx and SS@Lipo/Hb/GOx/JQ1. Furthermore, highly expressed GSDMD (Fig. 4C) verified that SS@Lipo/Hb/GOx/JQ1-mediated pyroptosis contributed to the superior antitumor efficacy as well as the improvement of tumor immunogenicity. Subsequently, immunofluorescence staining of CRT and immunohistochemical examination of HMGB1 in Fig. 4D and E showed the highest expression of CRT and HMGB1 in SS@Lipo/Hb/GOx and SS@Lipo/Hb/GOx/JQ1 groups. Although there was no difference for tumor immunogenicity between SS@Lipo/Hb/GOx and SS@Lipo/Hb/GOx/JQ1 treated cells in vivo and in vitro, SS@Lipo/Hb/GOx/JQ1 significantly increased CTLs infiltration and decreased PD-L1 expression compared with SS@Lipo/Hb/GOx, as shown in Fig. 4F and I. This

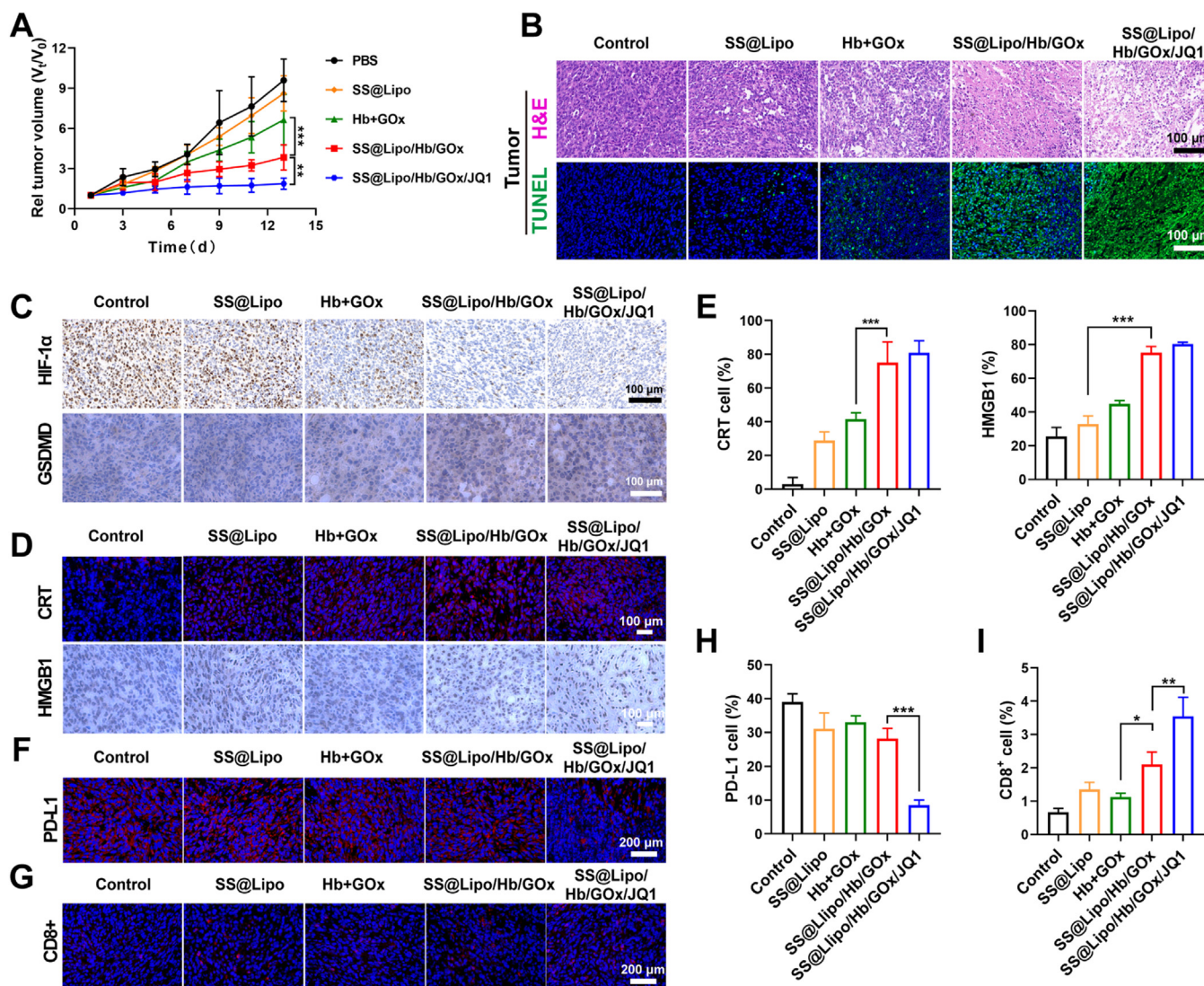


**Fig. 4 – (A)** Relative tumor volume ( $n = 5$ ; mean  $\pm$  SD). **(B)** Representative H&E and TUNEL staining images. **(C)** Immunohistochemical determination of HIF-1 $\alpha$  and GSDMD in tumor tissue. **(D, E)** Representative images **(D)** and corresponding quantitative analysis **(E)** of CRT and HMGB1 ( $n = 3$ ; mean  $\pm$  SD). **(F, H)** Immunohistochemical images **(F)** and quantitative analysis **(H)** of PD-L1 expressed in tumor sections ( $n = 3$ ; mean  $\pm$  SD). **(G, I)** CD8 expression in tumor site in different groups ( $n = 3$ ; mean  $\pm$  SD). P values were calculated by one-way or two-way ANOVA with a Tukey post-hoc test (\* $P < 0.05$ , \*\*  $P < 0.01$  and \*\*\*  $P < 0.001$ ).

was mainly due to the reason that JQ1 suppressed PD-L1 expression by inhibiting BRD4, relieving immunosuppression and augmenting immune response.

### 3.6. In vivo immunoregulation of SS@Lipo/Hb/GOx/JQ1

To further investigate antitumor immune response, tumor-infiltrating immune cells were analyzed via flow cytometry. The ratio of mature DCs (CD40+CD86+) in SS@Lipo/Hb/GOx group (~17.4 %) and SS@Lipo/Hb/GOx/JQ1 group (~20.4 %) was significantly increased compared with the control group (~3.4 %) (Fig. 5A), which was mainly due to that ROS induced antigens release and elicited immune response in vivo. In addition, percentage of tumor-infiltrating CD8+ T lymphocytes in SS@Lipo/Hb/GOx/JQ1 group was 1.3-, 2.8- and

1.7-fold higher than that of SS@Lipo/Hb/GOx, Hb+GOx and SS@Lipo groups, respectively (Fig. 5B). As vital suppressive cells, Tregs are capable of exhausting effector immune cells characterized by high level of PD-L1 [47]. After treatment with different formulations, the ratio of Tregs (CD25+ Foxp3+) in tumor tissue was investigated. Fig. 5C demonstrated that Tregs in SS@Lipo/Hb/GOx/JQ1 group were much lower than that of other groups, consistent with PD-L1 expression. The results further confirmed that JQ1 with PD-L1 inhibition function could suppress immune evasion and overcome adaptive immune resistance, paving the way for cancer immunotherapy. Next, serum cytokines, including IFN- $\gamma$ , IL-6 and TNF- $\alpha$ , were further examined via ELISA. By comparison, secretion of these immunological enhancement cytokines was significantly increased after treatment with

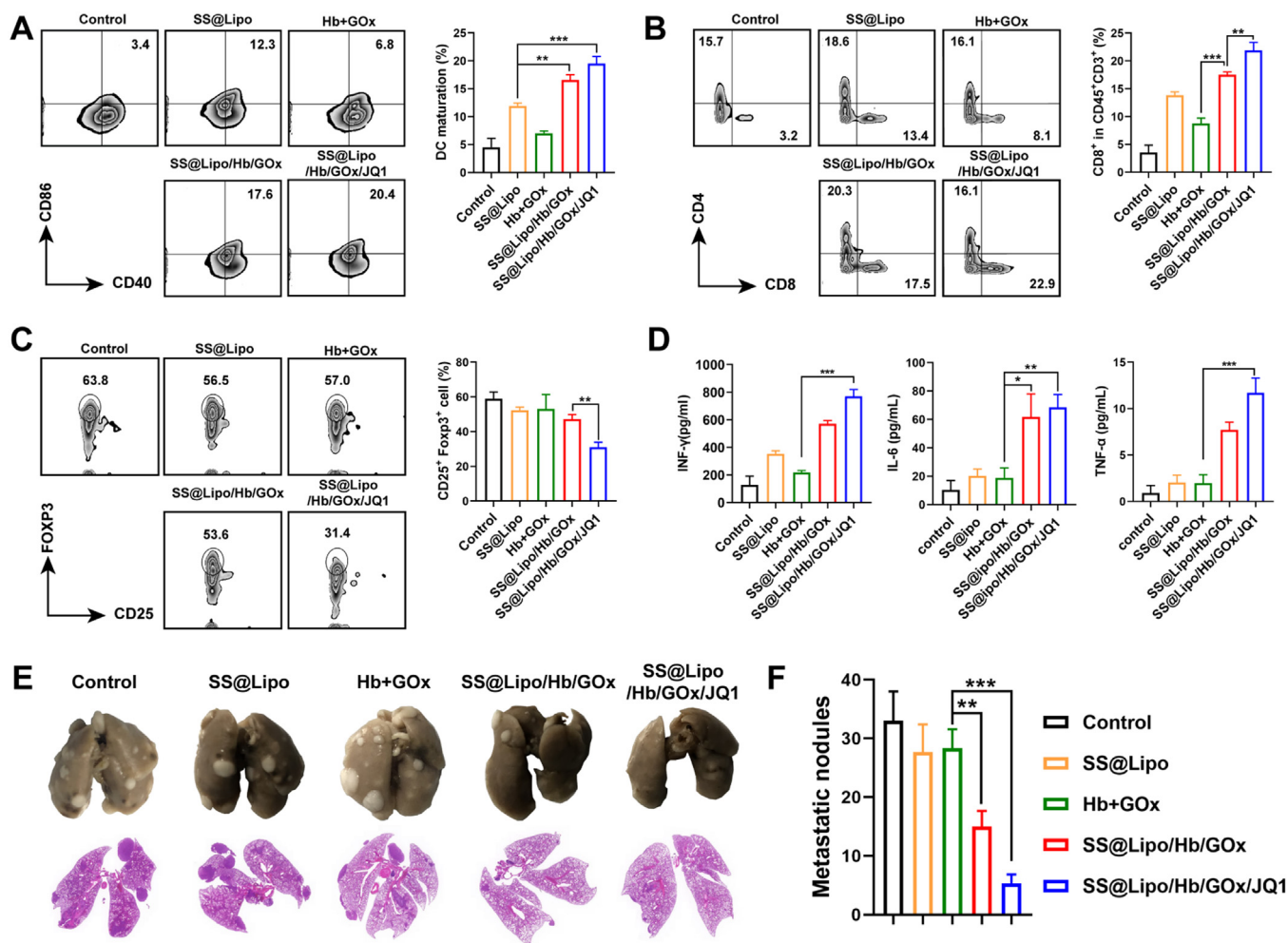


**Fig. 5 – (A-C) Flow cytometry analysis of immune cells: (A) Matured DCs (CD11c+CD86+CD40+), (B) CD8+ T cells (CD45+CD3+CD8+), and (C) Tregs (CD45+CD11b+CD25+Foxp3+). (D) Immunostimulatory cytokines IFN- $\gamma$ , IL-6 and TNF- $\alpha$ . (E) Photograph and H&E sections of lung tissues. (F) Quantification of pulmonary metastatic nodules after different treatments. Data are presented as mean  $\pm$  SD ( $n = 3$ );  $P$  values were calculated by one-way ANOVA with a Tukey post-hoc test (\* $P < 0.05$ , \*\*  $P < 0.01$  and \*\*\*  $P < 0.001$ ).**

drugs-loaded nanoparticles, especially SS@Lipo/Hb/GOx/JQ1 (Fig. 5D).

Next, immune effector cells (mature DCs and CTLs) in lymph nodes (LNs) were analyzed to assess systemic immune activation. According to Fig. S22, CD40+CD86+ DCs population increased in SS@Lipo/Hb/GOx and SS@Lipo/Hb/GOx/JQ1 groups, demonstrating that coexistence of antigens and adjuvant could activate APCs more effectively. Correspondingly, SS@Lipo/Hb/GOx/JQ1 treatment increased CTLs in LNs and the frequency of CD8+ T cells was  $\sim 2.2$ -fold higher than that of control group (Fig. S23), implying high immune response for tumor elimination. After mice received treatments similar to the in vivo antitumor study, lung tissues were collected for imaging and H&E staining. The results in Fig. 5E showed that metastatic nodules in lung were observed in mice with Saline, SS@Lipo and Hb+GOx treatments. Quantitative analysis showed that metastatic nodules in SS@Lipo/Hb/GOx/JQ1 group were 6.2-fold lower than that of control group (Fig. 5F), implying the potential

of SS@Lipo/Hb/GOx/JQ1 induced immune response for metastasis rejection.

#### 4. Conclusion

In summary, based on the discovery that total SS exhibited excellent tumor targeting ability and adjuvant activity inheriting from parent spore, we developed a biomimetic spore nanoplatform synergistic BMAT, CDT and immunotherapy for cancer treatment. Lipo/Hb/GOx activated potent immune response by enhancing tumor immunogenicity. Simultaneously, acting as immune adjuvants, PNG and Mn in SS promoted antigen processing/presentation through TLR2 and cGAS-STING signaling pathways, respectively. Moreover, the down-regulation of PD-L1 via JQ1 and hypoxia alleviation by Hb synergistically reshaped immunosuppressive TME, paving the way for T cell-based antitumor immunity. In

vitro and in vivo investigation consistently indicated that the synergistic treatment effect of SS@Lipo/Hb/GOx/JQ1 permitted significant inhibition ability on primary tumors and lung metastasis, which could hardly be realized by BMAT, CDT and immunotherapy alone. Collectively, SS@Lipo/Hb/GOx/JQ1 might be an optimum strategy to potentiate immune activation and provide therapeutic potential for cancer treatment.

### Conflicts of interest

The authors report no conflicts of interest. The authors alone are responsible for the content and writing of this article.

### Acknowledgements

This work was supported by the National Natural Science Foundation of China (No. 82272847, 82202318, 82304417, 82303529), The Henan Province Fund for Cultivating Advantageous Disciplines (No. 222301420012), Central Plains science and technology innovation leading talent project (No. 234200510005), The project tackling of key scientific and technical problems of Henan Province (No. 232102311163), China Postdoctoral Science Foundation (2022TQ0310, 2023TQ0307, 2023M730971).

### Supplementary materials

Supplementary material associated with this article can be found, in the online version, at [doi:10.1016/j.ajps.2024.100912](https://doi.org/10.1016/j.ajps.2024.100912).

### REFERENCES

- [1] Siegel RL, Miller KD, Wagle NS, Jemal A. Cancer statistics 2023. *CA-Cancer J Clin* 2023;73(1):17–48.
- [2] Zhao H, Li Y, Shi H, Niu M, Li D, Zhang Z, et al. Prodrug nanoparticles potentiate tumor chemo-immunometabolic therapy by disturbing oxidative stress. *J Control Release* 2022;352:909–19.
- [3] Lou X, Chen Z, He Z, Sun M, Sun J. Bacteria-mediated synergistic cancer therapy: small microbiome has a big hope. *Nanomicro Lett* 2021;13(1):37.
- [4] Wu Y, Li J, Zhong X, Shi J, Cheng Y, He C, et al. A pH-sensitive supramolecular nanosystem with chlorin e6 and triptolide co-delivery for chemo-photodynamic combination therapy. *Asian J Pharm* 2022;17(2):206–18.
- [5] Sang W, Zhang Z, Dai Y, Chen X. Recent advances in nanomaterial-based synergistic combination cancer immunotherapy. *Chem Soc Rev* 2019;48(14):3771–810.
- [6] Yap TA, Parkes EE, Peng W, Moyers JT, Curran MA, Tawbi HA. Development of immunotherapy combination strategies in cancer. *Cancer Discov* 2021;11(6):1368–97.
- [7] Xie YJ, Huang M, Li D, Hou JC, Liang HH, Nasim AA, et al. Bacteria-based nanodrug for anticancer therapy. *Pharmacol Res* 2022;182:106282.
- [8] Zheng C, Song Q, Zhao H, Kong Y, Sun L, Liu X, et al. A nanoplatform to boost multi-phases of cancer-immunity-cycle for enhancing immunotherapy. *J Control Release* 2021;339:403–15.
- [9] Zhang Z, Liu X, Chen D, Yu J. Radiotherapy combined with immunotherapy: the dawn of cancer treatment. *Signal Transduct Target Ther* 2022;7(1):258.
- [10] Xu C, Li SY, Chen JT, Wang HM, Li Z, Deng QY, et al. Doxorubicin and erastin co-loaded hydroxyethyl starch-polycaprolactone nanoparticles for synergistic cancer therapy. *J Control Release* 2023;356:256–71.
- [11] Li J, Luo Y, Pu K. Electromagnetic nanomedicines for combinational cancer immunotherapy. *Angew Chem Int Ed* 2021;60(23):12682–705.
- [12] Duan F, Jin W, Zhang T, Zhang F, Gong L, Liu X, et al. Self-activated cascade biocatalysis of glucose oxidase-polycation-iron nanoconjugates augments cancer immunotherapy. *ACS Appl Mater Inter* 2022;14(29):32823–35.
- [13] Yang A, Sun Y, Lyu B, Chen B, Fan Z, Li M, et al. One-pot preparation of nanodispersion with readily available components for localized tumor photothermal and photodynamic therapy. *Asian J Pharm* 2022;17(1):120–8.
- [14] Fu LH, Qi C, Sun T, Huang K, Lin J, Huang P. Glucose oxidase-instructed biomineralization of calcium-based biomaterials for biomedical applications. *Exploration* 2023;3(6):20210110.
- [15] Zhou H, Zhou YL, Mao JA, Tang LF, Xu J, Wang ZX, et al. NCOA4-mediated ferritinophagy is involved in ionizing radiation-induced ferroptosis of intestinal epithelial cells. *Redox Biol* 2022;55:102413.
- [16] Gao W, Wang X, Zhou Y, Wang X, Yu Y. Autophagy, ferroptosis, pyroptosis, and necroptosis in tumor immunotherapy. *Signal Transduct Target Ther* 2022;7(1):196.
- [17] Tang Z, Liu Y, He M, Bu W. Chemodynamic therapy: tumour microenvironment-mediated fenton and fenton-like reactions. *Angew Chem Int Ed* 2019;58(4):946–56.
- [18] Tang Z, Zhao P, Wang H, Liu Y, Bu W. Biomedicine meets fenton chemistry. *Chem Rev* 2021;121(4):1981–2019.
- [19] Fang X, Wu X, Li Z, Jiang L, Lo WS, Chen G, et al. Biomimetic anti-PD-1 peptide-loaded 2D FePSe<sub>3</sub> nanosheets for efficient photothermal and enhanced immune therapy with multimodal MR/PA/thermal imaging. *Adv Sci* 2021;8(2):2003041.
- [20] Yang Y, Zuo S, Li L, Kuang X, Li J, Sun B, et al. Iron-doxorubicin prodrug loaded liposome nanogenerator programs multimodal ferroptosis for efficient cancer therapy. *Asian J Pharm* 2021;16(6):784–93.
- [21] Kalia VC, Patel SKS, Cho BK, Wood TK, Lee JK. Emerging applications of bacteria as antitumor agents. *Semin Cancer Biol* 2022;86:1014–25.
- [22] Zhang J, Hansen LG, Gudich O, Viehrig K, Lassen LMM, Schruëbbers L, et al. A microbial supply chain for production of the anti-cancer drug vinblastine. *Nature* 2022;609(7926):341–7.
- [23] Yang Z, Zhu Y, Dong Z, Hao Y, Wang C, Li Q, et al. Engineering bioluminescent bacteria to boost photodynamic therapy and systemic anti-tumor immunity for synergistic cancer treatment. *Biomaterials* 2022;281:121332.
- [24] Liu Y, Lu Y, Ning B, Su X, Yang B, Dong H, et al. Intravenous delivery of living listeria monocytogenes elicits gasdmermin-dependent tumor pyroptosis and motivates anti-tumor immune response. *ACS Nano* 2022;16(3):4102–15.
- [25] Lee SH, Cho SY, Yoon Y, Park C, Sohn J, Jeong JJ, et al. Bifidobacterium bifidum strains synergize with immune checkpoint inhibitors to reduce tumour burden in mice. *Nat Microbiol* 2021;6(3):277–88.
- [26] Wang W, Xu H, Ye Q, Tao F, Wheeldon I, Yuan A, et al. Systemic immune responses to irradiated tumours via the transport of antigens to the tumour periphery by injected flagellate bacteria. *Nat Biomed Eng* 2022;6(1):44–53.
- [27] Zhai Y, Ma Y, Pang B, Zhang J, Li Y, Rui Y, et al. A cascade targeting strategy based on modified bacterial vesicles

- for enhancing cancer immunotherapy. *J Nanobiotechnology* 2021;19(1):434.
- [28] Cheng K, Zhao R, Li Y, Qi Y, Wang Y, Zhang Y, et al. Bioengineered bacteria-derived outer membrane vesicles as a versatile antigen display platform for tumor vaccination via Plug-and-Display technology. *Nat Commun* 2021;12(1):2041.
- [29] Zhou M, Tang Y, Xu W, Hao X, Li Y, Huang S, et al. Bacteria-based immunotherapy for cancer: a systematic review of preclinical studies. *Front Immunol* 2023;14:1140463.
- [30] Liu Y, Niu L, Li N, Wang Y, Liu M, Su X, et al. Bacterial-mediated tumor therapy: old treatment in a new context. *Adv Sci* 2023;10(12):e2205641.
- [31] Wong CC, Yu J. Gut microbiota in colorectal cancer development and therapy. *Nat Rev Clin Oncol* 2023;20(7):429–52.
- [32] Song Q, Zheng C, Jia J, Zhao H, Feng Q, Zhang H, et al. A probiotic spore-based oral autonomous nanoparticles generator for cancer therapy. *Adv Mater* 2019;31(43):e1903793.
- [33] Garcia-Diaz A, Shin DS, Moreno BH, Saco J, Escuin-Ordinas H, Rodriguez GA, et al. Interferon receptor signaling pathways regulating PD-L1 and PD-L2 expression. *Cell Rep* 2019;29(11):3766.
- [34] Hu Y, Lin L, Guo Z, Chen J, Maruyama A, Tian H, et al. In situ vaccination and gene-mediated PD-L1 blockade for enhanced tumor immunotherapy. *Chin Chem Lett* 2021;32(5):1770–4.
- [35] Dorand RD, Nthale J, Myers JT, Barkauskas DS, Avril S, Chirieleison SM, et al. Cdk5 disruption attenuates tumor PD-L1 expression and promotes antitumor immunity. *Science* 2016;353(6297):399–403.
- [36] Song Q, Zhao H, Zheng C, Wang K, Gao H, Feng Q, et al. A bioinspired versatile spore coat nanomaterial for oral probiotics delivery. *Adv Funct Mater* 2021;31(41):2104994.
- [37] Griffin ME, Espinosa J, Becker JL, Luo JD, Carroll TS, Jha JK, et al. Enterococcus peptidoglycan remodeling promotes checkpoint inhibitor cancer immunotherapy. *Science* 2021;373(6558):1040–6.
- [38] Wang C, Guan Y, Lv M, Zhang R, Guo Z, Wei X, et al. Manganese increases the sensitivity of the cGAS-STING pathway for double-stranded DNA and is required for the host defense against DNA viruses. *Immunity* 2018;48(4):675–87.
- [39] Di Lorenzo A, Bolli E, Ruiu R, Ferrauto G, Di Gregorio E, Avalle L, et al. Toll-like receptor 2 promotes breast cancer progression and resistance to chemotherapy. *Oncoimmunology* 2022;11(1):2086752.
- [40] Yang Z, Wen J, Wang Q, Li Y, Zhao Y, Tian Y, et al. Sensitive, real-time, and *in-vivo* oxygen monitoring for photodynamic therapy by multifunctional mesoporous nanosensors. *ACS Appl Mater Inter* 2019;11(1):187–94.
- [41] Lin LS, Huang T, Song J, Ou XY, Wang Z, Deng H, et al. Synthesis of copper peroxide nanodots for H<sub>2</sub>O<sub>2</sub> self-supplying chemodynamic therapy. *J Am Chem Soc* 2019;141(25):9937–45.
- [42] Zeng Y, Zhou H, Ding J, Zhou W. Cell membrane inspired nano-shell enabling long-acting Glucose Oxidase for Melanoma starvation therapy via microneedles-based percutaneous delivery. *Theranostics* 2021;11(17):8270–82.
- [43] Niu Q, Liu Y, Zheng Y, Tang Z, Qian Y, Qi R, et al. Co-delivery of nigericin and decitabine using hexahistidine-metal nanocarriers for pyroptosis-induced immunotherapeutics. *Acta Pharm Sin B* 2022;12(12):4458–71.
- [44] Peng S, Xiao F, Chen M, Gao H. Tumor-microenvironment-responsive nanomedicine for enhanced cancer immunotherapy. *Adv Sci* 2022;9(1):e2103836.
- [45] Wang B, Zhao Q, Zhang Y, Liu Z, Zheng Z, Liu S, et al. Targeting hypoxia in the tumor microenvironment: a potential strategy to improve cancer immunotherapy. *J Exp Clin Cancer Res* 2021;40(1):24.
- [46] Sheng J, Wu J, Yin X, Sun Z, Wang X, Zhang J, et al. Synergetic treatment of oxygen microcapsules and lenvatinib for enhanced therapy of HCC by alleviating hypoxia condition and activating anti-tumor immunity. *Chin Chem Lett* 2023;34(4):107738.
- [47] Zhou F, Gao J, Xu Z, Li T, Gao A, Sun F, et al. Overcoming immune resistance by sequential prodrug nanovesicles for promoting chemoimmunotherapy of cancer. *Nano Today* 2021;36:101025.